Crystal to quasicrystal surface phase transition: an unlocking mechanism for templated growth

Davide Curcio,[†] Elisa Miniussi,[†,‡] Paolo Lacovig,[¶] Silvano Lizzit,[¶] Rosanna Larciprete,[§] Joseph A. Smerdon,[‖,⊥] Vinod R. Dhanak,[‖] Ronan McGrath,[‖] and Alessandro Baraldi[*,†,¶,#]

Physics Department, University of Trieste, Via Valerio 2, 34127 Trieste, Italy, present address: Physik Institut der Universität Zürich, Winterthurerstrasse 190, 8057 Zürich, Switzerland, Elettra-Sincrotrone Trieste S.C.p.A., Strada Statale 14 Km 163.5, 34149 Trieste, Italy, CNR-Institute for Complex Systems, Via Fosso del Cavaliere 100, 00133 Roma, Italy, Department of Physics, University of Liverpool, Oxford Street, L69 7ZE, Liverpool UK, present address: Jeremiah Horrocks Institute of Mathematics, Physics and Astronomy, University of Central Lancashire, Preston PR1 2HE, UK, and IOM-CNR, Laboratorio TASC, AREA Science Park, S.S. 14 km 163.5, 34149 Trieste, Italy

E-mail: alessandro.baraldi@elettra.eu

Abstract

[*]To whom correspondence should be addressed

[†]Physics Department, University of Trieste, Via Valerio 2, 34127 Trieste, Italy

[‡]present address: Physik Institut der Universität Zürich, Winterthurerstrasse 190, 8057 Zürich, Switzerland

[¶]Elettra-Sincrotrone Trieste S.C.p.A., Strada Statale 14 Km 163.5, 34149 Trieste, Italy

[§]CNR-Institute for Complex Systems, Via Fosso del Cavaliere 100, 00133 Roma, Italy

[‖]Department of Physics, University of Liverpool, Oxford Street, L69 7ZE, Liverpool UK

[⊥]present address: Jeremiah Horrocks Institute of Mathematics, Physics and Astronomy, University of Central Lancashire, Preston PR1 2HE, UK

[#]IOM-CNR, Laboratorio TASC, AREA Science Park, S.S. 14 km 163.5, 34149 Trieste, Italy

In this experimental work we have studied and characterized a surface phase transition on a decagonal $Al_{72}Ni_{11}Co_{17}$ sample between a crystalline phase, which is induced by sputtering with energetic noble gas ions, and the bulk-like decagonal phase. The surface transition to the stable, quasicrystalline phase was followed as a function of temperature by two complementary techniques: High-Resolution X-Ray Photoelectron Spectroscopy (HR-XPS) and Low Energy Electron Diffraction (LEED). The observation of shifts in the core-electron binding energies of the constituent atoms and of other photoemission line shape parameters as the surface undergoes the phase transition, and the comparison with the structural information obtained from the LEED data, enabled us to determine the evolution of the surface from 5 twinned cubic crystalline domains to the decagonal phase. A quasicrystalline chemical environment with some degree of long range order is observed for Al before the quasicrystalline surface is fully recovered, pointing to a two-step reordering process, where two sublattices order separately at different temperatures. Strong modifications in the valence band are reflected in the core level binding energies, and the observed reduction in density of states at the Fermi energy for the decagonal phase is consistent with a Hume-Rothery stabilization mechanism

Introduction

Quasicrystals (QC) have attracted an incredible amount of attention and debate since their discovery in 1982, which revolutionized the field of modern crystallography.[1] There are still many issues that are unsolved for this class of solids~~This class of solids is still largely unexplored~~ due to their difficult theoretical description, since most computational methods heavily rely on periodicity, and also from the experimental point of view, because the complicated nature of quasicrystal structures poses many technical challenges. Among the most peculiar properties of QCs many arise from the unique atomic configurations in the very first few atomic layers.[2–5] Concerning the electronic structure, the presence of a pseudogap

in the surface band structure has been largely debated.[6,7] While Hard x-ray photoemission measurements with mean escape lengths larger than 100 Å performed on icosahedral fivefold AlPdMn and AlCuFe QCs[8] show that the pseudogap is enhanced in the quasicrystalline bulk in the case of icosahedral phases, more surface sensitive low energy photoemission measurements do not observe such a pronounced pseudogap.[9–11] Similarly, numerical simulations have shown that a broad pseudogap is present in decagonal AlNiCo, although it is shallower at the surface than in the bulk.[12] On the other hand, it has been shown[13] that the pseudogap is mostly absent for vacuum cleaved and for sputtered surfaces, but it is recovered after annealing to high temperatures. Also, extremely surface sensitive STS experiments, have shown that a deep pseudogap is present on the surface of a decagonal AlNiCo QC.[14] ~~Hard x-ray photoemission measurements performed on icosahedral fivefold AlPdMn and AlCuFe QCs solved this controversial issue, [8] showing that the pseudogap is enhanced in the quasicrystalline bulk in the case of icosahedral phases, contrarily to what is observed in surface sensitive low energy photoemission [9–11] because of a symmetry breaking effect caused by the surface.~~ On many QCs, what still remains elusive is the relationship between the electronic properties and the symmetry/composition of the surface when the latter evolves from a crystalline overlayer to quasi-periodic order. This is a key issue for this class of solids, where the phase stabilization is believed to be caused by the Hume-Rothery (H-R) mechanism,[7,15,16] where the interaction between the Fermi sphere and the quasi-Brillouin zone favors the quasiperiodic phase instead of the periodic approximants by stabilizing specific atomic clusters with prohibited rotational symmetry.[15] Very recent theoretical and experimental works,[17,18] show how, for decagonal QCs, the long-range order during QC growth is enforced by phason strain relaxation, rather than by non-local interactions, and that the clusters stabilized by the H-R mechanism overlap obeying specific rules only as a consequence of the growth mechanism. However, the case of templated QC growth, as in the conversion of a crystalline overlayer to a quasiperiodic, bulk-like surface, might move many of these complications aside, as the nearly perfect quasiperiodic order is enforced by the substrate

templating effect and does not need to emerge spontaneously. A common phenomenon that occurs during the preparation of QC surfaces can be exploited for this purpose. In fact, in order to achieve a high degree of surface cleanliness and smoothness, QCs first have to be sputtered with energetic noble gas ions and then annealed at high temperature for extended amounts of time, usually of the order of hours.[19] The sputtering procedure typically changes the surface composition of Al-based QCs, and eventually causes a surface phase transition to a crystalline structure that can be reconverted to a QC surface upon annealing.[20–25] Although a combination of diffraction-based and photoemission experimental techniques has allowed the understanding that the formation of quasicrystalline periodicity is accompanied by significant changes in the surface composition,[23] the temperature dependent effects on the electronic properties resulting from the structural changes are not clear yet. Knowledge of the link between the electronic and geometric structure of QCs when they form at high temperature could be extremely important at the fundamental level[26] and for practical applications[27], also in the fields of plasmonics[28] and catalysis.[29] In order to clarify these issues and gain insight into the phase transition from a crystalline to a quasicrystalline phase, we used temperature programmed x-ray photoelectron spectroscopy (TP-XPS[30]) to monitor the temperature evolution of a layer with cubic crystalline structure obtained after sputtering an AlNiCo QC surface. By exploiting the high brilliance of the soft x-ray radiation produced at third generation synchrotron light sources and the high data acquisition rate achievable by the experimental workstation it was possible to collect an extended set of core level (Co $2p_{3/2}$, Ni $2p_{3/2}$, and Al 2p) and valence band spectra while annealing the sputtered AlNiCo up to the transition temperature to the QC phase. This strategy allowed us to understand that the phase transition from sputter-induced crystalline structure to QC is only partially driven by the activation of successive diffusion mechanisms, and that the temperature activated unlocking of two sublattices, which are predicted to order separately at different temperatures by Monte Carlo simulations,[17] may play an important role in the phase transition. The formation of the QC phase is directly linked to a depression in the density of states (DOS)

at the Fermi levelenergy (E_F): the shift of the Ni and Co more-than-half-full d bands to higher BE during the phase transition is accompanied by a reduction of the Al p and s states, giving altogether a smaller DOS at E_F, consistently with the H-R stabilization mechanism.

Experimental

The d-AlNiCo(00001) (henceforth AlNiCo) single grain quasicrystal, with bulk composition $Al_{72}Ni_{11}Co_{17}$The d-$Al_{72}Ni_{11}Co_{17}$(00001) (henceforth AlNiCo) single grain quasicrystal was about 5 mm in size and was mounted on a liquid nitrogen cryostat manipulator with 4 degrees of freedom. The sample was cooled by liquid nitrogen and heated by electron bombardment from hot W filaments mounted behind it. The temperature of the sample was monitored by means of two K-type thermocouples spotwelded close to the sample. The photoemission experiments were carried out in the ultra high vacuum (UHV) chamber (base pressure 1×10^{-10} mbar) of the SuperESCA beamline at the Elettra synchrotron radiation facility (Trieste, Italy). The spectra were collected by means of a Phoibos 150 mm mean radius hemispherical electron energy analyzer from SPECS, using a lens mode with an acceptance angle of $\pm 7°$ in the non dispersing direction, equipped with an in-house developed delay-line detector. The experimental setup combines high energy resolution with high data acquisition rates, thus allowing real-time monitoring of the evolution of the core-level spectral components over a wide temperature range.[31] The high-resolution core level spectra were acquired with photon energies of 230 eV for Al 2p, 950 eV for Ni $2p_{3/2}$ and Co $2p_{3/2}$, and 100 eV for Valence Band (VB) spectra. The photon energy was chosen in such a way that the photoionization cross-section was maximized, while ensuring a comparable mean escape depth for all photoelectrons, such that 90% of the signal comes from the first 6-8 atomic layers.[32] In order to calibrate the exact binding energy (BE) scale, every XPS spectrum has been referenced to the Fermi edge of a polycrystalline Mo plate holding the AlNiCo sample. The overall experimental energy resolution, which accounts for both the

electron energy analyzer and the x-ray monochromator, was kept within 50 meV for measurements at 100 eV and 230 eV photon energies, and within 150 meV for measurements at 950 eV photon energy, as determined by probing the spectral width at the Fermi edge of a Mo polycrystal. Doniach-Šunjić (D-S) functions[33] with a Shirley-type background[34] were fitted to all the core level spectra to obtain the line shape parameters and to determine the intensity and binding energy. The line shape parameters of these functions reflect physical quantities: the Lorentzian width describes peak broadening due to the finite lifetime of the core hole excited final state, the Gaussian width is related to the phonon-induced spectral broadening, and to the experimental resolution, the asymmetry is linked to the electron-hole pair excitation probability, and reflects the local electronic DOS at the Fermi edge for any atom in a specific chemical environment.[35] Thus, this parameter enables the identification of the atoms that most strongly contribute to the DOS at E_F. The VB spectra have been acquired at normal emission, along the crystallographic direction shown in the Supporting Information Fig. S1. The used acceptance angle of $\pm 7°$ ensures that each energy bin of the detector integrates about $2\,\text{Å}^{-1}$ of reciprocal space centered around the Γ point. This, together with the high degree of symmetry of all the surfaces studied, implies that the VB spectra measured are a good approximation of an integral over the whole Brilluoin Zone and that our analysis gives parameters relevant for the description of the evolution of the DOS near the Fermi edge. The VB spectra were quantitatively analyzed by fitting a parabola to the the spectra in a 1.3 eV interval around E_F, in agreement with previous STS studies, where a pronounced parabolic pseudogap centered at E_F has been observed.[14] The function $\{[a + b(E - E_F)^2] f(E - E_F)\} * G(E)$ was fitted to the photoemission spectrum, with $f(x)$ being the Fermi-Dirac distribution, $G(x)$ the normal distribution (to account for the experimental resolution and thermal broadening), a and b the parameters that describe the pseudogap shape. This widely used model for the shape of the VB spectrum close to the Fermi edge gives a convenient way of determining the shape of the pseudogap with a single parameter. Indeed, the parameter a is representative of the DOS at the Fermi level, while

the b/a ratio quantifies the depth and width of the pseudogap. Quasicrystal surfaces consistently tend to have larger b/a ratios than their approximants or the periodic surfaces of the same quasicrystals.~~a Fermi function multiplied by a linear DOS to the photoemission spectrum in a small energy range around E_F. This model works quite well, in agreement with Ref. [36] who observed a metallic Fermi edge for a similar QC.~~ Selected VB spectra and fit results are show in the Supporting Information, Fig. S2. An arbitrary Lorentzian shape is usually employed to model the depression in the DOS commonly found in QCs near the Fermi edge,[37] while in other cases a metallic edge has been observed[36], but in our case a parabolic DOS model was found to give high quality fits.~~linear DOS was found to better approximate the shape of the Fermi edge in a 700 meV interval around E_F.~~ The low energy electron diffraction (LEED) experiments were carried out in the UHV chamber (base pressure 1×10^{-10} mbar) of the Surface Science Laboratory at Elettra–Sincrotrone Trieste, where a commercial Fisons LEED instrument with a transfer width of about 160 Å (at energies between 27 eV and 71 eV) was employed. The AlNiCo sample was grown at the Ames laboratory using the melt decantation method,[38] and was cut exposing the decagonal (10000) face. Its stoichiometry is consistent with the basic Co-rich (b-Co) structure in the AlNiCo phase diagram.[39] The in-vacuum preparation consists of repeated cycles of Ar^+ sputtering and annealing to 1100 K for 120 minutes. The sputtering was performed at a glancing angle of 20°, with a 1.5 keV Ar^+ ions and a sample drain current of 10 μA. The long annealing times are required both to reorder the quasicrystal structure after sputtering, and to re-establish the surface stoichiometry, since the Ar^+ bombardment generally targets more efficiently the lighter atoms in alloys[24,40] (Al in the present case). This changes the surface stoichiometry and pushes the QC over the stability limits in its phase diagram, causing a surface phase transition to a periodic, non quasicrystalline structure, a phenomenon which is known to happen on most Al-based QCs. The decagonal, quasicrystalline AlNiCo phase is recovered after annealing to 1100 K. High energy resolution spectra were also measured at 80 K after sputtering the sample and annealing to selected temperatures (in the range 80–1090 K) in

a similar fashion to what has been performed in the LEED experiments. Examples of high resolution spectra acquired after annealing to selected temperatures and cooling to 80 K, and spectra from the time resolved series extracted at the corresponding temperatures, together with the fit results and individual components as obtained from the fits, are shown in Fig. S3 (Supporting Information). Although in principle the different experimental procedure might influence the evolution of the phase transition, the similarity of the high resolution spectra when compared to those from the annealing ramp, apart from thermal broadening, confirms that the two experimental procedures give similar results.

Results

Structural Characterization: Low Energy Electron Diffraction

For the LEED images, we analyzed the position, the intensity, and the FWHM of non-equivalent diffraction spots, as an indicator of the surface structure quality and of the long-range order. This was accomplished by fitting 2D Gaussian functions to the LEED images in a very limited square area around the spot.

At low temperature, after sputtering, the diffraction pattern (Fig. 1(a), top-left) indicates the presence of a surface with cubic *B2* structure (CsCl-like, *i.e.* two inter-penetrating primitive cubic cells, whose corners are occupied by Al and transition metal atoms, respectively), with (110) orientation, exhibiting 5 twinned domains. The lattice parameter was found to be (2.90 ± 0.04) Å by comparison with calibration LEED images acquired for an Ir(111) surface. This value should be compared with the CoAl and NiAl *B2* lattice constants, which are 2.86 Å and 2.89 Å, respectively.[41,42] In order to obtain structural information on the phase transition from the *B2* structure to the bulk-like QC surface, we investigated the changes in the LEED pattern as a function of annealing temperature and sputtering time. In each experiment the clean, freshly prepared sample was exposed to an Ar^+ sputtering cycle at 300 K for 20 or 60 minutes, and annealed in steps of 100 K from 370 K to 1070 K.

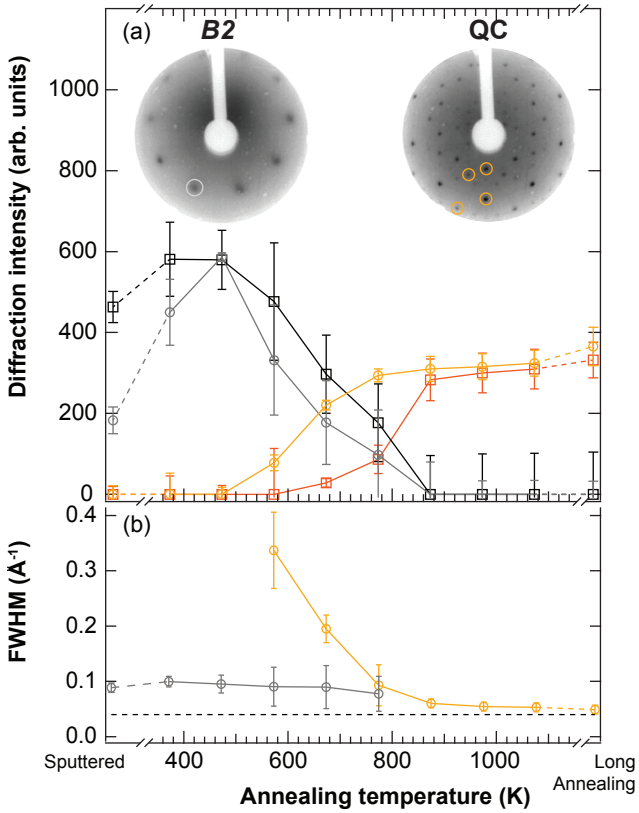

Figure 1: LEED diffraction spot parameters as a function of annealing temperature during the phase transition. In (a) the sum of the intensities of selected diffraction spots at 27 eV for the *B2* structure (gray) and at 64 eV for the QC structure (orange) as a function of annealing temperature, after sputtering for 20 minutes (lighter colors, circles) and for 60 minutes (darker colors, squares). In (b), the average FWHM of the selected diffraction peaks at 46 eV as a function of annealing temperature. The dashed line in (b) shows the k value corresponding to the transfer width of the instrument (160 Å at 46 eV, corresponding to 0.04 $Å^{-1}$ in reciprocal space).

The measurements were taken at the end of each annealing step after cooling to 300 K. The electron energies were chosen so that the relevant structure's spots have maximum intensity, namely 27 eV to maximize the intensity of the *B2* diffraction pattern, 64 eV to maximize the intensity of the QC diffraction pattern. We also investigated how the full width at half maximum (FWHM) evolves as a function of temperature for the 20 minute sputtering time. In this case, the electron energy of 46 eV was chosen to have both structures visible across the phase transition. This way, the transfer width can be consistently compared to the FWHM of spots from both structures. However, cooling to 80 K for image acquisition was

necessary because of the low intensity of the spots at this energy, and because of the high background contribution from disorder during the phase transition. Cooling the sample to 80 K allows the quenching of the phonon contributions, giving both brighter spots and lower background. For the FWHM the formula for the domain size $L = 2\pi/FWHM$ [43] still applies to quasicrystals, and by using a quasilattice parameter of 0.26 $Å^{-1}$ [44] (this value is reported in the $a \cdot a^* = 1$ convention) one can label the diffraction spots. Our analysis returned a set of relevant parameters as a function of increasing annealing temperature, both from the crystalline and quasi-crystalline structures. The integrated intensity (Fig. 1(a)) provides information on the number of in-phase scatterers, and therefore on the ordering of the surface. In the temperature range between 770 K and 870 K the *B2* phase disappears. Longer sputtering times do not influence the upper temperature limit for the *B2* phase existence, although the *B2* spots are always brighter for longer sputtering times. On the other hand, the QC spots appear at lower temperatures for shorter sputtering times~~On the other hand, the QC spots appear earlier for shorter sputtering times~~, namely between 470 K and 570 K for 20 minutes of sputtering, and between 570 K and 670 K for 60 minutes of sputtering. These differences, however, do not seem to have an influence on the intensity of the spots after a 2 h annealing, as expected for the fully recovered quasicrystal surface. Also, the spot width analysis, reported in Fig. 1(b), shows a stable FWHM for the *B2* diffraction spots, suggesting that the mean domain size of the *B2* nanocrystals is of about 60 Å and remains constant for increasing temperatures. Similar crystallite sizes have been found for growth of few-layer Al on $Al_{70}Co_{15}Ni_{15}$ [45]. The FWHM for the QC spots reaches the instrumental limit at 870 K. From Fig. 1(b) it can be seen how the quasicrystal domains become detectable in LEED when they reach about 20 Å in average size, and as the annealing temperature increases, they grow to become larger than the transfer width of the instrument. The effects of the long 2 h annealing described in the Experimental Section are also reflected in the LEED data, as can be seen in the small increase in diffraction intensity (Fig. 1(a)).

High energy resolution core level photoemission results: characterization of the clean quasicrystal surface

After preparing the surface by sputtering and annealing, the sample was cooled to 80 K and spectra of the Al 2p (Fig. 2(a)), Ni $2p_{3/2}$ (Fig. 2(b)), and Co $2p_{3/2}$ (Fig. 2(c)) core levels were acquired. In the case of Ni $2p_{3/2}$ and Co $2p_{3/2}$, a single component D-S function fits the data well: the normalized residuals (the residuals divided by the square root of the counts in each energy channel) do not show any modulation and the value is always within the expected limit for statistical noise.

The Al 2p spectrum can be described reasonably well by two spin-orbit components, although the normalized residuals show modulations larger than 3, which can be explained by the superposition of a finite number of closely spaced components that are described with a Gaussian broadening of the fitting function. In our case, the Gaussian broadening describes the 4 or more inequivalent nearest neighbor configurations~~In our case, the Gaussian broadening describes the 4 or more [46] inequivalent chemical environments~~ experienced within a single QC layer by the Al atoms involved in the photoemission process and includes the contribution of surface relaxation and surface core level shift effects that should result in a very large number of photoemission peaks, which cannot be resolved individually even with 50 meV resolution. The line shape parameters and BEs of the Al 2p spectrum (reported in Table 1) can be compared to the values obtained for the Al(111) surface.[47] The binding energies of the Al $2p_{3/2}$ and Al $2p_{1/2}$ core levels in the QC are, respectively, 72.62 eV and 73.04 eV, shifted by 80 meV towards lower binding energies with respect to the Al(111) 2p core levels. Comparing the line shape, the most obvious difference is a much larger FWHM for the QC core level spectra (290 meV in the QC, to be compared with 100 meV for Al(111)). This is mainly due to Gaussian contribution (the Lorentzian widths being smaller than 80 meV). The same comparison with the elemental metal counterparts can be drawn also for the transition metal core levels, Ni $2p_{3/2}$ and Co $2p_{3/2}$, whose spectra for our AlNiCo sample are reported in Fig. 2(b) and (c), respectively, and whose line shape parameters are

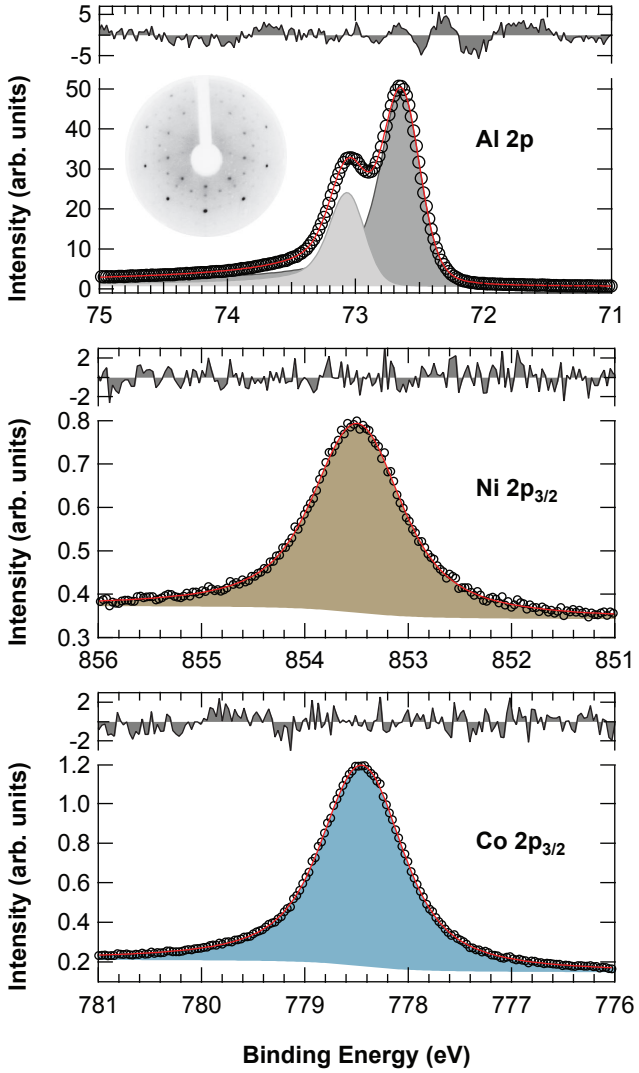

Figure 2: Core level spectra of Al 2p, Ni $2p_{3/2}$, and Co $2p_{3/2}$ acquired for the clean AlNiCo sample surface. Fit results (continuous lines) are also shown superimposed on the experimental data (empty circles), as well as the single peak components as determined by the fits (shaded). Fitting residuals normalized to the Poisson statistics are plotted above each spectrum, with a scale in standard deviation units. A LEED pattern (77 eV) of the QC surface for which the spectra were acquired is shown in the inset.

also reported in Table 1. For the Ni $2p_{3/2}$ core level we find a BE of 853.49 eV, up-shifted by 0.9 eV~~1.1 eV~~ with respect to Ni metal (852.6 eV[48]). The Gaussian width of 530 meV is much larger than the experimental contribution. The Co $2p_{3/2}$ core level (with a BE of 778.45 eV) is also shifted by 350 meV to higher BE with respect to metallic Co (778.1 eV[48]). This behavior can be explained in terms of the H-R stabilization mechanism, as the shift of

the *d*-bands to higher BEs will lead to a corresponding shift of the core levels.[49] The larger Gaussian widths compared to the metallic counterparts are evidence of the several chemical environments present for each atomic species.

Table 1: Fitting parameters for Al 2p, Ni $2p_{3/2}$ and Co $2p_{3/2}$ core levels taken on the clean QC surface.

Fitting Parameter	Co $2p_{3/2}$	Ni $2p_{3/2}$
Lorentzian width	(650 ± 10) meV	(730 ± 10) meV
Asymmetry	0.0 ± 0.1	0.0 ± 0.1
Gaussian width	(510 ± 10) meV	(530 ± 10) meV
Binding energy	(778.45 ± 0.01) eV	(853.49 ± 0.01) eV
	Al $2p_{3/2}$	Al $2p_{1/2}$
Lorentzian width	(80 ± 10) meV	(30 ± 10) meV
Asymmetry	0.11 ± 0.01	0.11 ± 0.01
Gaussian width	(290 ± 10) meV	(290 ± 10) meV
Binding energy	(72.62 ± 0.01) eV	(73.04 ± 0.01) eV

High energy resolution core level photoemission results: characterization of the *B2* to QC phase transition

In order to gain direct information on the phase transition, we employed TP-XPS during the annealing process. After sputtering the sample with 1.5 keV Ar^+ for 20 minutes to induce the surface transition to the crystalline *B2* phase, the temperature was linearly ramped from 330 K to 930 K at a rate of 0.5 K/s. Real time, *in-situ* XPS spectra were acquired every 10 s during the annealing, resulting in a 5 K difference between spectra. The Al 2p, Ni $2p_{3/2}$, and Co $2p_{3/2}$ core level and VB spectra, were followed during the phase transition, in order to monitor the alloy composition and the surface electronic structure modifications.

The series of time lapsed spectra (about 200 for each annealing process) is shown in Fig. 3(b,g,l), with the x-axis representing the electron BE of each spectrum, the y-axis representing the annealing temperature, and using a color scale proportional to the intensity. ~~High energy resolution spectra were measured at 80 K after sputtering the sample and~~

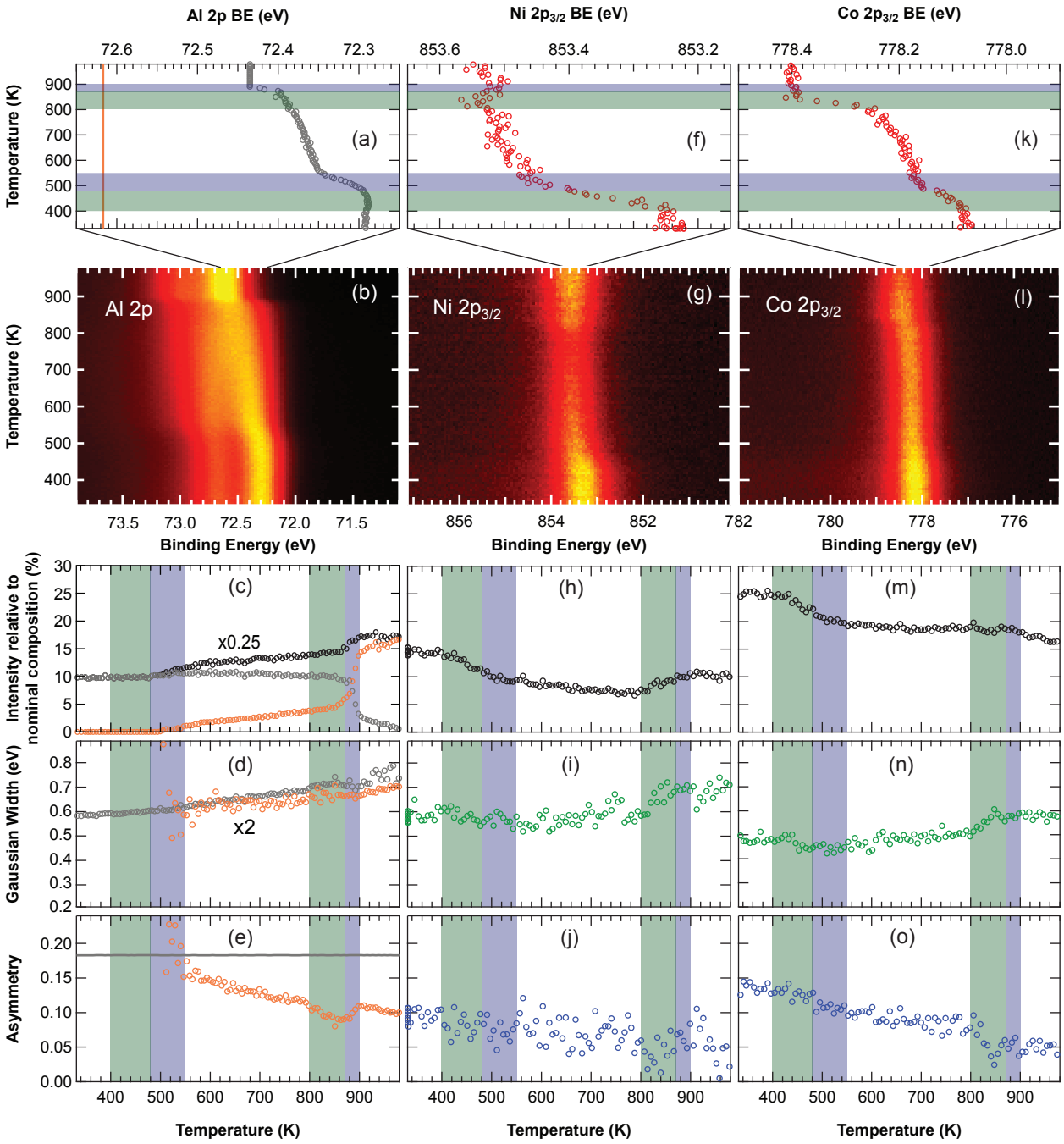

Figure 3: TP-XPS spectra for Al 2p (b), Ni $2p_{3/2}$ (g), and Co $2p_{3/2}$ (l) core levels. The spectra were acquired *in-situ* and fitted with D-S functions, thus obtaining a set of temperature dependent parameters. These are the binding energy (a, f, k), the peak integral (c, h, m), the Gaussian width (d, i, n), and the asymmetry parameter (e, j, o). For the Al 2p core levels, the specific values pertaining to the different surface species present are plotted separately (QC orange, *B2* gray). The temperature ranges TM1 (green, 400–480 K), AL1 (blue, 480–550 K), TM2 (green, 800–870 K), and AL2 (blue, 870–900 K), are highlighted.

~~annealing to selected temperatures (in the range 80–1090 K) in order to guide the analysis of the TP-XPS experiments. In fact, the smaller Gaussian component at low temperature and the higher sampling resolution of the data allows for a more precise determination of the other parameters.~~ The Al 2p spectrum measured at temperatures below 500 K shows a single doublet Al $2p^{B2}$ (3/2 component at 72.29 eV). Above 500 K it was possible to identify two sets of spin-orbit split peaks, as evidenced by a large deviation of the degeneracy ratio from the expected value of 0.5 (using only one spin-orbit couple in the fit results in a value of 1.8). The new doublet, at the same binding energy as that of the surface Al 2p doublet after the final annealing (3/2 component at 72.62 eV), was assigned to the QC structure (Al $2p^{QC}$). For the Al 2p core level small spectral changes can be appreciated. The time resolved series (Fig. 3(b)) has two marked temperature regions where major changes take place, the first one from 480 K to 550 K (AL1 range), the second one from 870 K to 900 K (AL2 range). Also, above 500 K, the Al $2p^{QC}$ core levels first appear. The intensity of the Al $2p^{B2}$ doublet initially increases in the AL1 temperature range (Fig. 3(c)), and slowly decreases subsequently, while the intensity of the Al $2p^{QC}$ components gradually increases from when it first appears at 500 K up to 870 K. In the AL2 temperature range, the spectral weight of the Al $2p^{QC}$ and Al $2p^{B2}$ components swaps. The total Al 2p signal tends to rise with increasing temperature, with a steeper increase in the AL2 range. The BE of the Al $2p^{B2}$ (Fig. 3(a)), besides a continuous up-shift with the annealing temperature, increases by ∼60 meV in AL1, and by ∼40 meV in AL2, reaching an overall shift of ∼150 meV. The asymmetry parameter of the Al $2p^{QC}$ is found to start at 0.18 and to continuously drop to 0.1 at 880 K. A small increase of the Al $2p^{QC}$ component asymmetry is observed in the temperature range AL2, but by 980 K the value of 0.1 is recovered. Fig. 3(f-j) shows a similar analysis for the Ni $2p_{3/2}$ core level. The temperature ranges where relevant changes take place (see Supporting Information Table S1 for a quick reference) are TM1 (400–480 K), and TM2 (800–870 K). In TM1, the Ni $2p_{3/2}$ integral intensity (Fig. 3(h)) drops to about 75% of the initial value. Between TM1 and TM2, a clear decreasing trend is also observed, while in

TM2 the intensity is partially recovered. The Ni $2p_{3/2}$ BE (Fig. 3(f)) also exhibits a marked shift to higher values in TM1 and remains stable in TM2. The overall change in BE is of about 300 meV. The Gaussian width (Fig. 3(i)) only shows the expected increasing trend as the temperature grows. The asymmetry (Fig. 3(j)), on the other hand, displays a general trend towards lower values as the temperature is increased. The relatively large noise for the Ni $2p_{3/2}$ Gaussian width and asymmetry parameter are due to to the reduced flux the beamline has at 950 eV photon energy, together with the relatively small cross section for Ni at this photon energy. Fig. 3(l) reports the evolution of the Co $2p_{3/2}$ core level as a function of annealing temperature. In Fig. 3(m) the integral intensity shows a marked drop in the TM1 temperature range, as for the Ni $2p_{3/2}$ level. A slight trend to lower intensities above TM1 is observed also for the Co $2p_{3/2}$ core level. The BE (Fig. 3(k)) exhibits two large shifts to higher values, the first in TM1, the second in TM2, bringing the total BE shift to about 330 meV. As observed for Nickel, the Gaussian width (Fig. 3(n)) shows an increase compatible with phonon broadening and the asymmetry parameter shows a trend towards smaller values (Fig. 3(o)) eventually becoming about 1/3 the initial value.

The VB spectra, shown in Fig. 4(a), have been fitted around the Fermi level, and the parameters a and b/a obtained from the fits are plotted in Fig. 4(b). ~~DOS at E_F is plotted in Fig. 4(b)~~. The valence band, like the core levels, undergoes relevant changes during the annealing ramp. VB spectra acquired at 80 K after sputtering and after the subsequent 120 min annealing are shown in the Supporting Information Fig. S4. In the temperature range AL1, an increase in the intensity of the s and p VB states leads to a somewhat higher a parameter, implying a higher DOS at E_F. The largest changes occur between 800 K and 900 K, in correspondence of the TM2 and AL2 temperature ranges. The s and p states display a large drop in intensity, in great part behaving like the Al $2p^{B2}$ doublet intensity, while the maximum location of the d-bands displays a net shift of about 340 meV to higher BE. Also, the b/a parameter shows a marked increase from a value of 2 to a value of 3.5, indicating that the pseudogap has undergone a transition to a more quasicrystalline-like

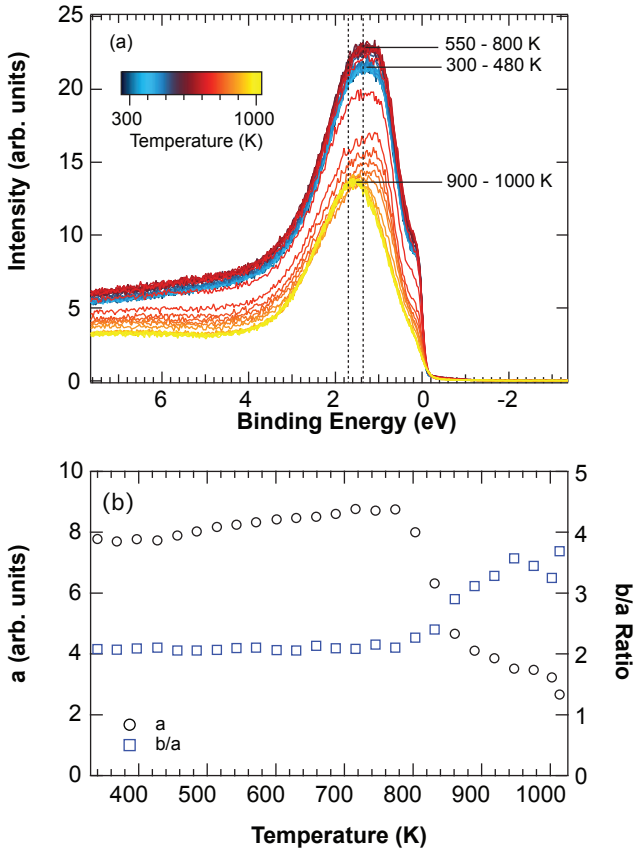

Figure 4: Evolution of the VB (a) and of the parameters a and b/a derived from the fits~~and of the density of states at the E_F~~ (b) as a function of annealing temperature, after sputtering the clean AlNiCo surface. The dotted lines in (a) show the BE of maximum for the d bands, at 1.36 eV for the sputtered surface, and at 1.70 eV for the completely annealed surface.

shape.

Discussion

In order to deepen the understanding of the link between structural and electronic evolution during the phase transition, we considered the temperature evolution of the different parameters extracted from the core and valence level spectral analysis and the surface composition. Fig. 5 reports the Al, Ni, and Co concentrations from the sputtered surface going through the phase transition to the QC structure. In order to derive the surface composition during the phase transition, the temperature resolved integrals were calibrated by integrat-

ing the high resolution spectra acquired for the clean, freshly prepared surface of known stoichiometry (0.72 for Al 2p, 0.11 for Ni $2p_{3/2}$ and 0.17 for Co $2p_{3/2}$), and calculating the relative normalization factors. The temperature resolved spectra were further normalized by the total intensity at each temperature, so that the curves are always representative of the relative composition. It should be noted that, since the calibration was performed on the clean, freshly prepared surface following a 120 min annealing, the surface composition at the end of the annealing ramp is close, but not exactly equal, to that of the bulk.

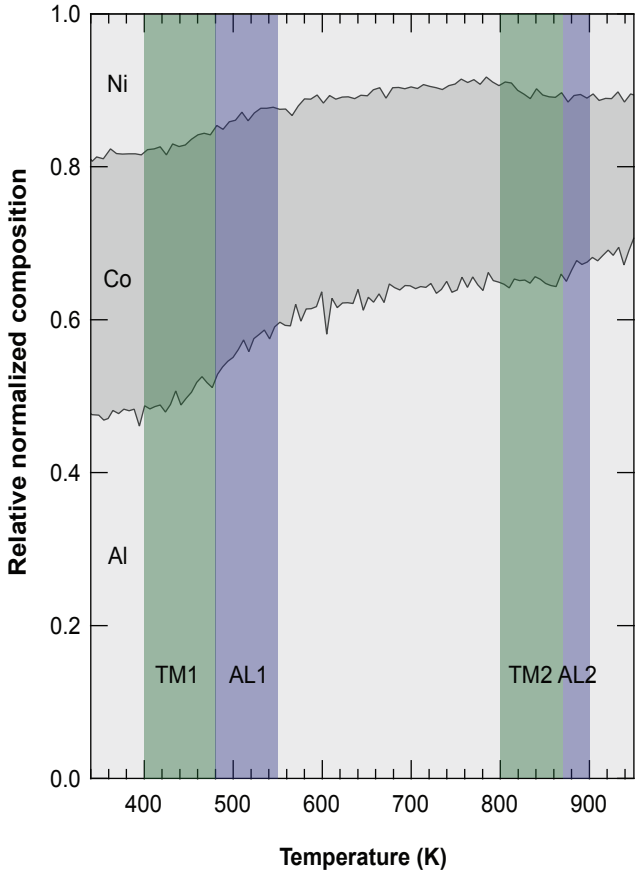

Figure 5: Plot of the normalized intensities for the Al 2p, Ni $2p_{3/2}$, and Co $2p_{3/2}$ core levels as a function of annealing temperature, after the sputtering-induced formation of the *B2* phase. The width of each band is representative of the relative surface concentration of each element during the phase transition. The temperature ranges TM1 (green, 400–480 K), AL1 (blue, 480–550 K), TM2 (green, 800–870 K), and AL2 (blue, 870–900 K), are highlighted.

At 300 K, after sputtering, the composition is compatible with that of the (Ni,Co)-rich side of the *B2* phase ($Al_{0.47}(Ni,Co)_{0.53}$), consistently with the LEED patterns. The limited

size (about 60 Å) of the $B2$ crystallites we have observed is likely due to a phenomenon similar to that observed in the case of epitaxial growth of Al(111) on a decagonal AlNiCo quasicrystal[45]. In this case, the limited size is due to the fact that there is a critical adsorbate size at which a commensurate growth breaks down for the Al nanocrystals. This system is expected to behave structurally like NiAl: in the (Ni,Co)-rich side of the *B2* phase, the excess transition metals are accommodated by antisite defects (with the Ni and Co atoms taking the place of Al in the cubic lattice), while for the Al-rich composition, the dominant defect type is a transition metal structural vacancy.[50] Regarding the individual diffusion coefficients for Ni and Co in the $B2$ phase, we observe that the ratio in intensity for the two species changes as a function of temperature (see Supporting Information, Fig. S5), implying a different diffusion coefficient for Ni and Co in Al(Ni,Co). This ratio starts from a value close to the nominal bulk stoichiometry ratio (17/11), as is expected because of the very similar sputtering efficiencies of the two chemical species, and recovers to this value after the phase transition is complete. The composition evolution during the annealing ramp reveals 3 distinct stages, marked by changes in the relative atomic concentrations towards the bulk composition. In the first stage, from 400 K up to 550 K, we first observe Ni and Co bulk diffusion during TM1, with very little change in the Al $2p^{B2}$ intensity. This is consistent with a behavior previously observed for NiAl,[50] where, for the Ni-rich composition, the intrinsic diffusion coefficient of Ni is much higher than that of Al. At 480 K the composition is close to $Al_{50}(Ni,Co)_{50}$ (see Fig. 5). Above this temperature Ni and Co diffusion is dramatically slowed, and the Al-rich region of the *B2* phase is accessed. The different type of defects, and therefore the different diffusion mechanism, favors the diffusion of the majority species, as implied by the reported self-diffusion coefficients.[50] The growth of the Al $2p^{B2}$ during AL1 implies that Al fills a portion of the vacancies left by Ni and Co downward diffusion. The changes in chemical environment of the atoms in the *B2* phase determines a shift to higher BE of Al $2p^{B2}$, Ni $2p_{3/2}$, and Co $2p_{3/2}$ during TM1 and AL1. Also, at 500 K the emergence of the Al $2p^{QC}$ doublet, at the same BE as the Al 2p doublet in the clean QC, implies that

some of the Al atoms experience, at least locally, a quasicrystalline environment. Between AL1 and TM2 a second stage can be identified. The surface is generally less ordered and slowly evolves to a high point defect density configuration, compatibly with the observed continuous change in stoichiometry, so that the *B2* LEED spots keep getting fainter, while the background becomes more intense. At the same time, QC grains are observed to grow, receiving Al atoms both from the *B2* nanocrystals and from the bulk. At this point (within the TM2 and AL2 temperature intervals), a third phase can be identified. Transition metal 3*d* states shift to higher BE, and the Co $2p_{3/2}$ core level binding energy shifts in the same direction. The Ni concentration and Ni $2p_{3/2}$ BE also approach their final values, giving a clear indication that the transition metals are now found in a quasicrystalline environment. At 870 K (the onset of AL2), a dramatic change in the Al 2p spectrum marks the final event of the phase transition. The spectral weight almost completely shifts to the Al $2p^{QC}$, leaving only a small contribution from the Al $2p^{B2}$ component. Also, a marked increase in the total Al intensity can be noticed (Fig. 3(c)), and a small increase in Al $2p^{QC}$ asymmetry is observed. This behavior is compatible with a phase transition, where the bulk stoichiometry is approached very rapidly, and the increased degree of order could allow for a different efficiency in the core-hole screening from the quasicrystalline Al VB electrons.[51] This two-step growth of the QC structure is not understandable simply in terms of having enough available thermal energy to overcome diffusion barriers, since the diffusion of Al, Ni, and Co is active in the *B2* phase already at 500 K,[52] and the diffusion of Al, Ni, and Co is significant already at temperatures above 670 K in the AlNiCo decagonal QC.[23] Recent Monte Carlo simulations[17] suggest that decagonal QCs possess two sublattices: the *L*-sublattice, with decagonal clusters of about 32 Å in size that overlap so that the centers are 18.8 Å apart, and the *S*-sublattice, with decagonal clusters 11.6 Å apart, closer by a factor τ (the golden mean). The simulations imply that these sublattices order separately at different temperatures (with the *S*-sublattice unlocking at lower temperature with respect to the *L*-sublattice). Also, recent experimental work[18] has shown how decagonal AlNiCo quasicrystals grow by frequent

error-and-repair processes, suggesting that the long-range order is imposed, rather than by long-range interactions, by a phason strain relief mechanism, where deformations of the lattice planes~~lattice plains~~, which add to the system energy, are spontaneously corrected. This framework is capable of describing the two-step reordering process we observe: when the temperature is high enough for unlocking the S-sublattice, locally quasicrystalline clusters form and migrate, slowly converting the *B2* structure to QC. Upon cooling, the templating effect of the substrate imposed by the phason strain relaxation generates long-range order in the S-sublattice, and the acquired LEED patterns show an ordered QC. When also the L-sublattice is unlocked, the conversion of the *B2* structure to QC is greatly accelerated, and the major phase transition event takes place. Regarding the electronic structure, the Co $2p_{3/2}$ and Ni $2p_{3/2}$ asymmetries are large in the *B2* metallic phase because the Ni and Co partially localized $3d$ states are found close to the E_F, giving a larger contribution to the screening charges involved in the photoemission process. Upon retrieval of the QC phase, these asymmetries shrink to very small values because the $3d$ states are shifted well below E_F, contributing very little to the DOS at E_F. The Al $2p^{QC}$ doublet also has an asymmetry that is half of that of the Al $2p^{B2}$ doublet, suggesting also in this case a smaller contribution to the DOS at E_F. The data presented above show how the DOS at the Fermi level~~energy~~ is deeply linked to quasiperiodic order, and how the pseudogap is present (even though not with Lorentzian shape). In fact, while observing a phase transition from periodic *B2* Al(Ni,Co) to QC decagonal AlNiCo, the Al VB states drop in intensity (Fig. 4(a)) even when Al concentration grows, as can be partially understood by considering the exchange in intensity between Al $2p^{B2}$ and Al $2p^{QC}$ (Fig. 3(c)), which have very different asymmetries (Fig. 3(e)), and therefore different contributions to the DOS at E_F. In fact, the a parameter, describing the DOS at E_F, displays~~the DOS at E_F displays~~ an evolution that strongly resembles that of the total intensity of the *B2* phase. Transition metal d states also shift to higher BE, compatible with a H-R stabilization mechanism. Furthermore, the b/a ratio exhibits a 75% increase that is taken as a clear fingerprint of a high-symmetry phase~~This is taken as the~~

~~clear fingerprint of a high-symmetry phase~~, in agreement also with the LEED patterns, and shows how for this decagonal alloy the pseudogap is quite pronounced despite the high surface sensitivity of our experiments. The Lorentzian shape of the pseudogap is not, in fact, an intrinsic property of quasicrystalline valence bands, but rather an empiric shape which describes well some icosahedral QC VBs.[8,36,37] A shift of the states from close to E_F to higher BE may have a stabilizing effect for a specific cluster independently from the pseudogap shape.

Conclusions

Using two complementary experimental techniques, LEED and XPS, we characterized the clean, well-ordered surface of a decagonal AlNiCo quasicrystal, both prior to and after sputtering with energetic Ar^+ ions. The phase transition induced by this process is reversible, and a phase transition back to the QC structure is found to happen between 500 K and 900 K. The driving forces behind the phase transition appear to be compatible with a temperature activated unlocking of two sublattices that order separately at different temperatures, although this speculation is still far from being established.~~The driving forces behind the phase transition appear to be linked to the temperature activated unlocking of two sublattices that order separately at different temperatures.~~ A pseudogap was found to appear in the surface DOS near the Fermi level, with a clear link to quasiperiodic order, though not with a Lorentzian shape. Likely, the symmetry breaking caused by the surface may somewhat reduce the observed pseudogap, as reported in previous experimental studies for icosahedral quasicrystals[11] and in theoretical studies for decagonal AlNiCo[12],~~as reported in previous studies for icosahedral quasicrystals [11]~~, although this effect may be less pronounced due to the plane-stacking nature of our decagonal quasicrystal structure. The knowledge gained on the phase transition could be exploited to perform new classes of experiments, with surfaces that can also undergo a phase transition to a completely different

substrate composition and symmetry.

Author Information

Corresponding Author

*E-mail: alessandro.baraldi@elettra.eu.

Notes

The authors declare no competing financial interest.

Acknowledgement

We acknowledge the financial support from MIUR through the project PRIN entitle "GRAF. Frontiers in graphene research: understanding and controlling advanced functionalities" (N.20105ZZYSE001) and from the University of Trieste through the program "Finanziamento di Ateneo per progetti di ricerca scientifica - FRA 2014". Ames Laboratory is acknowledged for the growth of the AlNiCo sample.

References

(1) Shechtman, D.; Blech, I.; Gratias, D.; Cahn, J. W. Metallic Phase with Long-Range Orientational Order and No Translational Symmetry. *Phys. Rev. Lett.* **1984**, *53*, 1951–1953.

(2) Thiel, P. A. Quasicrystal Surfaces. *Annu. Rev. Phys. Chem.* **2008**, *59*, 129–152.

(3) Jenks, C. J.; Thiel, P. A. Quasicrystals:ĂĽ A Short Review from a Surface Science Perspective. *Langmuir* **1998**, *14*, 1392–1397.

(4) Sharma, H. R.; Shimoda, M.; Tsai, A. P. Quasicrystal surfaces: structure and growth of atomic overlayers. *Adv. in Phys.* **2007**, *56*, 403–464.

(5) Park, J. Y.; Salmeron, M. Fundamental Aspects of Energy Dissipation in Friction. *Chem. Rev.* **2014**, *114*, 677–711.

(6) Hafner, J.; Krajčí, M. Electronic structure and stability of quasicrystals: Quasiperiodic dispersion relations and pseudogaps. *Phys. Rev. Lett.* **1992**, *68*, 2321–2324.

(7) Krajčí, M.; Hafner, J.; Mihalkovič, M. Are decagonal quasicrystals stabilized by a Hume-Rothery mechanism? *Europhys. Lett.* **1996**, *34*, 207.

(8) Nayak, J.; Maniraj, M.; Rai, A.; Singh, S.; Rajput, P.; Gloskovskii, A.; Zegenhagen, J.; Schlagel, D. L.; Lograsso, T. A.; Horn, K. et al. Bulk Electronic Structure of Quasicrystals. *Phys. Rev. Lett.* **2012**, *109*, 216403.

(9) Stadnik, Z. M.; Purdie, D.; Garnier, M.; Baer, Y.; Tsai, A. P.; Inoue, A.; Edagawa, K.; Takeuchi, S. Electronic Structure of Icosahedral Alloys Studied by Ultrahigh Energy Resolution Photoemission Spectroscopy. *Phys. Rev. Lett.* **1996**, *77*, 1777–1780.

(10) Wu, X.; Kycia, S. W.; Olson, C. G.; Benning, P. J.; Goldman, A. I.; Lynch, D. W. Electronic Band Dispersion and Pseudogap in Quasicrystals: Angular-Resolved Photoemission Studies on Icosahedral $Al_{70}Pd_{21.5}Mn_{8.5}$. *Phys. Rev. Lett.* **1995**, *75*, 4540–4543.

(11) Neuhold, G.; Barman, S. R.; Horn, K.; Theis, W.; Ebert, P.; Urban, K. Enhanced surface metallic density of states in icosahedral quasicrystals. *Phys. Rev. B* **1998**, *58*, 734–738.

(12) Krajčí, M.; Hafner, J.; Mihalkovič, M. *Ab initio* study of the surface of a decagonal Al-Co-Ni quasicrystal. *Phys. Rev. B* **2006**, *73*, 134203.

(13) Fournée, V.; Pinhero, P. J.; Anderegg, J. W.; Lograsso, T. A.; Ross, A. R.; Canfield, P. C.; Fisher, I. R.; Thiel, P. A. Electronic structure of quasicrystalline surfaces: Effects of surface preparation and bulk structure. *Phys. Rev. B* **2000**, *62*, 14049–14060.

(14) Mäder, R.; Widmer, R.; Gröning, P.; Steurer, W.; Gröning, O. Correlating scanning tunneling spectroscopy with the electrical resistivity of Al-based quasicrystals and approximants. *Phys. Rev. B* **2013**, *87*, 075425.

(15) Tsai, A. A test of Hume-Rothery rules for stable quasicrystals. *J. Non-Cryst. Solids* **2004**, *334–335*, 317–322.

(16) Mizutani, U.; Takeuchi, T.; Sato, H. Interpretation of the Hume-Rothery rule in quasicrystals and their approximants. *J. Non-Cryst. Solids* **2004**, *334–335*, 331–335.

(17) Kuczera, P.; Steurer, W. Cluster-Based Solidification and Growth Algorithm for Decagonal Quasicrystals. *Phys. Rev. Lett.* **2015**, *115*, 085502.

(18) Nagao, K.; Inuzuka, T.; Nishimoto, K.; Edagawa, K. Experimental Observation of Quasicrystal Growth. *Phys. Rev. Lett.* **2015**, *115*, 075501.

(19) McGrath, R.; Ledieu, J.; Cox, E. J.; Diehl, R. D. Quasicrystal surfaces: structure and potential as templates. *J. Phys.: Condens. Matter* **2002**, *14*, R119.

(20) Zhang, Z.; Feng, Y. C.; Williams, D. B.; Kuo, K. H. Crystalline surface layers on quasicrystals. *Philos. Mag. B* **1993**, *67*, 237–251.

(21) Zhang, H.; Urban, K. Radiation-induced transformation from the decagonal quasicrystalline phase to a CsCl-type phase in Al-Cu-Co(-Si). *Philos. Mag. Lett.* **1992**, *66*, 209–215.

(22) Qin, Y.; Wang, R.; Wang, Q.; Zhang, Y.; Pan, C. Ar+-ion-irradiation-induced phase transformations in an $Al_{70}Co_{15}Ni_{15}$ decagonal quasicrystal. *Philos. Mag. Lett.* **1995**, *71*, 83–90.

(23) Cecco, C.; Albrecht, M.; Wider, H.; Maier, A.; Schatz, G.; Krausch, G.; Gille, P. Surface structure induced by Ar+-bombardment of decagonal AlNiCo. *J. Alloys Compd.* **2002**, *342*, 437–440.

(24) Zurkirch, M.; Bolliger, B.; Erbudak, M.; Kortan, A. R. Structural transformations at the surface of the decagonal quasicrystal $Al_{70}Co_{15}Ni_{15}$. *Phys. Rev. B* **1998**, *58*, 14113–14116.

(25) Bolliger, B.; Erbudak, M.; Vvedensky, D. D.; Zurkirch, M.; Kortan, A. R. Surface Structural Transitions on the Icosahedral Quasicrystal $Al_{70}Pd_{20}Mn_{10}$. *Phys. Rev. Lett.* **1998**, *80*, 5369–5372.

(26) Steinhardt, P. J. Solid-state physics: How does your quasicrystal grow? *Nature* **2008**, *452*, 43–44.

(27) Dubois, J.-M. New prospects from potential applications of quasicrystalline materials. *Mater. Sci. Eng., A* **2000**, *294–296*, 4–9.

(28) Amin, M.; Khan, A. D. Polarization Selective Electromagnetic-Induced Transparency in the Disordered Plasmonic Quasicrystal Structure. *J. Phys. Chem. C* **2015**, *119*, 21633–21638.

(29) Gu, Y.-Q.; Fu, X.-P.; Du, P.-P.; Gu, D.; Jin, Z.; Huang, Y.-Y.; Si, R.; Zheng, L.-Q.; Song, Q.-S.; Jia, C.-J. et al. In Situ X-ray Diffraction Study of Co–Al Nanocomposites as Catalysts for Ammonia Decomposition. *J. Phys. Chem. C* **2015**, *119*, 17102–17110.

(30) Baraldi, A.; Comelli, G.; Lizzit, S.; Cocco, D.; Paolucci, G.; Rosei, R. Temperature programmed X-ray photoelectron spectroscopy: a new technique for the study of surface kinetics. *Surf. Sci.* **1996**, *367*, L67–L72.

(31) Baraldi, A.; Comelli, G.; Lizzit, S.; Kiskinova, M.; Paolucci, G. Real-time X-ray photoelectron spectroscopy of surface reactions. *Surf. Sci. Rep.* **2003**, *49*, 169–224.

(32) Tanuma, S.; Powell, C. J.; Penn, D. R. Calculations of electron inelastic mean free paths. *Surf. Interf. Anal.* **1994**, *21*, 165–176.

(33) Doniach, S.; Šunjić, M. Many-electron singularity in X-ray photoemission and X-ray line spectra from metals. *Journal of Physics C: Solid State Physics* **1970**, *3*, 285.

(34) Shirley, D. A. High-Resolution X-Ray Photoemission Spectrum of the Valence Bands of Gold. *Phys. Rev. B* **1972**, *5*, 4709–4714.

(35) Horn, K.; Theis, W.; Paggel, J. J.; Barman, S. R.; Rotenberg, E.; Ebert, P.; Urban, K. Core and valence level photoemission and photoabsorption study of icosahedral Al–Pd–Mn quasicrystals. *J. Phys.: Condens. Matter* **2006**, *18*, 435–448.

(36) Stadnik, Z. M.; Purdie, D.; Garnier, M.; Baer, Y.; Tsai, A.-P.; Inoue, A.; Edagawa, K.; Takeuchi, S.; Buschow, K. H. J. Electronic structure of quasicrystals studied by ultrahigh-energy-resolution photoemission spectroscopy. *Phys. Rev. B* **1997**, *55*, 10938–10951.

(37) Mori, M.; Matsuo, S.; Ishimasa, T.; Matsuura, T.; Kamiya, K.; Inokuchi, H.; Matsukawa, T. Photoemission study of an Al-Cu-Fe icosahedral phase. *J. Phys.: Condens. Matter* **1991**, *3*, 767.

(38) Fisher, I. R.; Kramer, M. J.; Islam, Z.; Ross, A. R.; Kracher, A.; Wiener, T.; Sailer, M. J.; Goldman, A. I.; Canfield, P. C. On the growth of decagonal Al-Ni-Co quasicrystals from the ternary melt. *Philos. Mag. B* **1999**, *79*, 425–434.

(39) Ritsch, S.; Beeli, C.; Nissen, H. U.; Gödecke, T.; Scheffer, M.; Lück, R. The existence regions of structural modifications in decagonal Al-Co-Ni. *Philos. Mag. Lett* **1998**, *78*, 67–75.

(40) Kelly, R. An attempt to understand preferential sputtering. *Nucl. Instrum. Methods* **1978**, *149*, 553–558.

(41) Vilars, P.; Calvert, L. D. *Pearson's handbook of crystallographic data for intermetallic phases*; American Society of Metals: Cleveland, OH, 1985.

(42) Taylor, A.; Doyle, N. J. Further studies on the nickel–aluminium system. I. β-NiAl and δ-Ni_2Al_3 phase fields. *J. Appl. Cryst.* **1972**, *5*, 201–209.

(43) Ertl, G.; Küppers, J. *Low energy electrons and surface chemistry*; VCH Verlagsgellschaft. Distribution, USA and Canada, VCH Publishers, 1985.

(44) Steurer, W.; Haibach, T.; Zhang, B.; Kek, S.; Lück, R. The structure of decagonal $Al_{70}Ni_{15}Co_{15}$. *Acta Crystallogr., Sect. B* **1993**, *49*, 661–675.

(45) Flückiger, T.; Weisskopf, Y.; Erbudak, M.; Lüscher, R.; Kortan, A. R. Nanoepitaxy: Size Selection in Self-Assembled and Oriented Al Nanocrystals Grown on a Quasicrystal Surface. *Nano Lett.* **2003**, *3*, 1717–1721.

(46) Ferralis, N.; Pussi, K.; Cox, E. J.; Gierer, M.; Ledieu, J.; Fisher, I. R.; Jenks, C. J.; Lindroos, M.; McGrath, R.; Diehl, R. D. Structure of the tenfold *d*-Al-Ni-Co quasicrystal surface. *Phys. Rev. B* **2004**, *69*, 153404.

(47) Nyholm, R.; Andersen, J. N.; van Acker, J. F.; Qvarford, M. Surface core-level shifts of the Al(100) and Al(111) surfaces. *Phys. Rev. B* **1991**, *44*, 10987–10990.

(48) Biesinger, M. C.; Payne, B. P.; Grosvenor, A. P.; Lau, L. W.; Gerson, A. R.; Smart, R. S. Resolving surface chemical states in XPS analysis of first row transition metals, oxides and hydroxides: Cr, Mn, Fe, Co and Ni. *Appl. Surf. Sci.* **2011**, *257*, 2717–2730.

(49) Citrin, P. H.; Wertheim, G. K.; Baer, Y. Core-Level Binding Energy and Density of States from the Surface Atoms of Gold. *Phys. Rev. Lett.* **1978**, *41*, 1425–1428.

(50) Paul, A.; Kodentsov, A.; van Loo, F. On diffusion in the β-NiAl phase. *J. Alloys Compd.* **2005**, *403*, 147–153.

(51) Hüfner, S.; Wertheim, G. K. Core-line asymmetries in the x-ray-photoemission spectra of metals. *Phys. Rev. B* **1975**, *11*, 678–683.

(52) Blum, R.-P.; Ahlbehrendt, D.; Niehus, H. Preparation-dependent surface composition and structure of NiAl(001): SPA-LEED and NICISS study. *Surf. Sci.* **1996**, *366*, 107–120.

Graphical TOC Entry

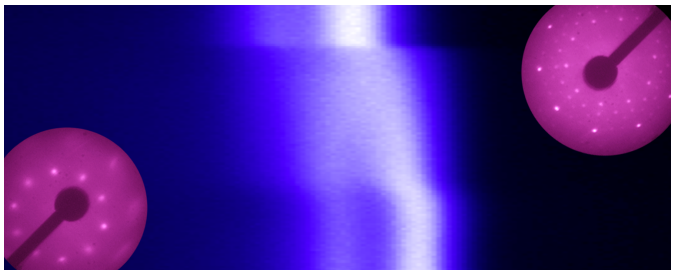

Selected results obtained for the temperature evolution of the sputtered AlNiCo surface, including Low Energy Electron Diffraction and a time-lapsed series of Al 2p High-Resolution Core Level Photoemission spectra.